Journal of Magnetic Resonance 211 (2011) 30–36

Contents lists available at ScienceDirect

Journal of Magnetic Resonance

journal homepage: www.elsevier.com/locate/jmr

Diffusion effects on longitudinal relaxation in poorly mixed compartments

J.R. Anderson [a], Q. Ye [a], J.J. Neil [b,c,d], J.J.H. Ackerman [a,b,e], J.R. Garbow [b,*]

[a] Department of Chemistry, Washington University, 1 Brookings Drive, St. Louis, MO 63130, USA
[b] Department of Radiology, Washington University School of Medicine, 660 South Euclid Ave., St. Louis, MO 63110, USA
[c] Department of Neurology, Washington University School of Medicine, 660 South Euclid Ave., St. Louis, MO 63110, USA
[d] Department of Pediatrics, Washington University School of Medicine, 660 South Euclid Ave., St. Louis, MO 63110, USA
[e] Department of Internal Medicine, Washington University School of Medicine, 660 South Euclid Ave., St. Louis, MO 63110, USA

ARTICLE INFO

Article history:
Received 13 February 2011
Revised 25 March 2011
Available online 1 April 2011

Keywords:
NMR
MRI
Flow
Thin slice
Semi-permeable fiber

ABSTRACT

Diffusion of spins between physical or virtual, communicating compartments having different states of longitudinal magnetization leads to diffusion-driven longitudinal relaxation. Herein, in two model systems, the effects of diffusion-driven longitudinal relaxation are explored experimentally and analyzed quantitatively. In the first case, longitudinal relaxation in a single slice of a water phantom is monitored spectroscopically as a function of slice thickness. In the second case, mimicking vascular flow/diffusion effects, longitudinal relaxation is monitored in a two-compartment, semi-permeable fiber phantom. In both cases, apparent longitudinal relaxation, though clearly multi-exponential, is well-modeled as bi-exponential.

1. Introduction

The remarkable performance capabilities of modern MR scanners are redefining the limits of spatial resolution, signal sensitivity, and data interpretation. Data are often of such high quality that subtle signal characteristics, ones that could previously be safely ignored, must now be recognized in accurate signal-modeling and parameter estimation. This is especially true when testing signal models against "ideal" data obtained from phantoms and phantom-like systems.

This laboratory has, for some time, been interested in signal models that describe systems characterized by coherent and incoherent displacement motions, e.g., flow, perfusion, and diffusion. Despite the multi-compartment complexity of most tissues, data modeling is typically performed using relatively simple mathematical representations of the signal. The utility of the resulting parametric maps depends upon the validity of the underlying simplifying assumptions, which can be difficult to assess. Recently, while pursuing control experiments with phantoms, we encountered diffusion-driven relaxation, a phenomenon that could, if unrecognized, compromise data interpretation.

Diffusion of spins between physical or virtual, communicating compartments having different states of longitudinal magnetization leads to diffusion-driven longitudinal relaxation [1–5]. The population of spins in one physical or virtual compartment will demonstrate altered longitudinal relaxation when exchanging, *via* diffusion, with a population of spins of different magnetization state from a communicating second compartment.

Herein, deviations from mono-exponential longitudinal relaxation due to diffusion-driven relaxation are examined in two limiting cases. In the first case, a sample consisting of a single physical compartment is divided, by slice selection, into two virtual compartments. Experiments are performed in which signal is only detected from one compartment – the selected slice. In the second case, a two-compartment, semi-permeable fiber phantom is constructed. Experiments are performed in which, due to time-of-flight flow effects, signal is only detected from one of the two compartments – the extra-lumenal compartment. The effects of diffusion between virtual and physical communicating compartments are observed and modeled, and the implications of diffusion-driven relaxation are discussed.

2. Materials and methods

2.1. Longitudinal relaxation rate constant determination

All longitudinal relaxation rate constants were measured with a modified fast inversion recovery (MFIR) pulse sequence [6]. MFIR is a variation on the standard inversion recovery experiment, in which images are collected at different inversion times (TI), where the repetition time (TR) is fixed at a value that is shorter than required for full recovery of longitudinal magnetization. This method realizes a portion of the time savings of fast inversion recovery

* Corresponding author.
E-mail address: garbow@wustl.edu (J.R. Garbow).

1090-7807/$ - see front matter © 2011 Elsevier Inc. All rights reserved.
doi:10.1016/j.jmr.2011.03.018

(FIR), for which both TI and TR are varied in concert in order to fix the pre-delay, but, unlike FIR, can be modeled even in the presence of imperfect flip angles by the following three parameter equation,

$$S(\mathrm{TI}) = A + B\exp(-R_1 \cdot \mathrm{TI}), \quad (1)$$

where S(TI) is the signal intensity for inversion time TI and R_1 is the longitudinal relaxation rate constant, the inverse of the time constant, T_1 [7,8].

Images and spectra were collected on scanners employing Oxford Instruments 4.7-T horizontal-bore magnets (Oxford Instruments; Oxford, UK) interfaced with Agilent/Varian DirectDrive™ consoles, and Agilent/Varian/Magnex gradient coil assemblies (Agilent Technologies, Santa Clara, CA, USA). All samples were positioned with the long axis of the sample (capillary tube) parallel to B_0. Experiments were carried out at the ambient temperature in the bore of the magnet (~21 °C).

2.2. Slice thickness experiments

Apparent longitudinal relaxation was monitored in a water-filled, 1.0-mm ID capillary tube *via* a slice-selective (transverse to the tube's long axis), spin-echo, MFIR spectroscopy experiment. To observe the effect of diffusion on the measurement, experiments were performed with four different slice thicknesses (TH): 1.00, 0.500, 0.250 and 0.125 mm. Crafted 90° and 180° pulses, similar in shape to Shinnar-Le Roux pulses, were used to minimize imperfections in slice profile [9,10]. To this same end, symmetric left and right crusher (''butterfly'') gradients were implemented with both the inversion and refocusing 180° pulses.

For all slice thicknesses, the acquisition parameters were: TR = 20.0 s, TE = 10.67 ms, and spectral width (SW) = 4006 Hz. To compare data at similar signal-to-noise ratio (SNR), the number of transients (NT) was varied: NT = 1 (TH = 1.00 mm), 4 (TH = 0.500 mm), 16 (TH = 0.250 mm), and 64 (TH = 0.125 mm). In addition, a single relaxation data set was acquired at higher SNR with TH = 10.0 mm and NT = 4, a slice thickness greater than the active region of the coil. Thirty logarithmically-spaced TI values ranging from 0.01 to 15 s were employed throughout.

Signal amplitudes were calculated from the total integrated intensity of the water ^{1}H resonance *via* in-house programs developed using Matlab (Mathworks; Natick, MA, USA). Relaxation data were modeled as exponential functions by Bayesian analysis methods developed in our lab (Bayesian Analysis of Common NMR Problems; http://bayesiananalysis.wustl.edu/index.html) [11,12].

2.3. Non-permeable and semi-permeable fiber phantom design

A non-permeable hollow fiber (polyurethane catheter; ID = 300 μm, OD = 400 μm) or semi-permeable hollow fiber (polysulfone dialyzer; ID = 200 μm, OD = 280 μm) was suspended through the middle of a capillary tube (ID = 1.0 mm) and held in place with epoxy applied at the ends of the capillary tube. (Note: in this paper, semi-permeable denotes a material allowing free diffusion of water and allowing, but potentially slowing, diffusion of aqueous Gd-based contrast agents; and non-permeable denotes a material completely blocking diffusion of both water and aqueous Gd-based contrast agents.) The phantom consisted of two physical compartments, the lumen, i.e., the interior of the fiber, and the extra-lumenal space, which includes the fiber wall and the extra-fiber region. The phantom design allowed controlled flow of media in the fiber lumen. The semi-permeable hollow fiber, similar to those used in hollow-fiber bioreactors, was harvested from a commercial dialyzer (Optiflux F-160NR; Fresenius Medical Care AG & Co., Bad Homburg, Germany). As the extra-lumenal space was closed and water is an incompressible fluid, there were no pressure gradients across the transverse axis of the phantom (i.e., between lumenal and extra-lumenal compartments).

Lumenal flow was achieved *via* a peristaltic pump. Flow rates were periodically measured just downstream of the phantom to assure constant flow velocities throughout the experiment.

2.4. Non-permeable and semi-permeable fiber phantom experiments

For both the semi-permeable and non-permeable fiber phantoms, T_1 maps were obtained with and without aqueous flow at 0 and 1 mM concentrations of Omniscan (gadodiamide; Gd-DTPA-BMA; GE Healthcare, Piscataway, USA). A flow rate of 0.4 mL/min was maintained during experiments requiring flow. If plug flow is assumed, this flow rate corresponded to a lumenal velocity of 0.2 mm/ms, translating to clearance of lumenal spins within TE/2 when TE = 10 ms and TH = 1 mm. Experiments with aqueous gadodiamide solution allowed sufficient equilibration time to ensure homogeneous distribution of gadodiamide (1 mM) throughout all compartments (i.e., the lumenal and extra-lumenal compartments had the same concentration of gadodiamide).

Four single-slice images (transverse to the fiber's long axis) were acquired to monitor longitudinal relaxation, with TI values 0.002, 0.080, 2.500, and 8.000 s for 0 mM gadodiamide experiments and 0.002, 0.025, 0.080, 0.250 s for 1 mM gadodiamide experiments. To ensure images at each TI had approximately the same SNR, variable numbers of transients (NT) were averaged for each image, corresponding, respectively, to the different TI values: NT = 8, 16, 32, and 8. To assure that no steady-state transverse magnetization was present during the MFIR experiment, the shortest value of Δ = TR − TI was set equal to three times the transverse relaxation time constant (T_2) of the bulk (non-flowing) solution: TR = 13.5 s for 0 mM gadodiamide experiments and 0.8 s for 1 mM gadodiamide experiments [8]. (Note: T_2 was measured independently for 0 mM and 1 mM gadodiamide solutions *via* spectroscopic methods with a standard CPMG sequence.) All images were acquired with the following parameters: TH = 1 mm; TE = 10 ms; in-plane field of view, 5.12×1.28 mm^2; in-plane voxel dimensions, 20×20 μm^2.

Modeling of the data was carried out using signal intensities from phased (absorption mode) images [13,14]. Parameters A, B, and R_1 (Eq. (1)) were estimated from the phased images by nonlinear least-squares analysis in Matlab. The image acquired at the longest TI was used for thresholding prior to modeling the relaxation data. R_1 values were only estimated for those voxels in which the signal intensity was greater than five times the standard deviation of the noise.

To identify regions corresponding to the fiber wall, proton-density weighted, gradient-echo images of the semi-permeable fiber phantom were acquired without flow (TR = 500 ms; TE = 9.7 ms; NT = 256; and flip angle, $\alpha = 20°$). These images were collected with the same field of view, slice thickness, and in-plane voxel dimensions as the images acquired for R_1 analysis.

A region of interest (ROI) consisting of voxels with different R_1 values would be expected to exhibit non-mono-exponential relaxation behavior. To examine this phenomenon, an ROI covering one sixteenth of the entire image (0.64×0.64 mm^2) was selected with the fiber at its center; lumenal voxels were discarded (976 voxels selected after thresholding). For each extra-lumenal voxel within the ROI, mono-exponential relaxation recovery curves (Eq. (1)) were derived based on the measured voxel intensities at the four TI values. These simulated relaxation recovery data sets, one for each voxel within the ROI, were averaged to derive a single relaxation recovery data set for the ROI as a whole, sampled at ten logarithmically-spaced TI values ranging from 0.017 to 15 s. Bayesian analysis was then applied to this derived, single ROI

relaxation data set to compare the probabilities of mono-, bi-, and tri-exponential models [11].

3. Results

3.1. Slice thickness experiments

As shown in Fig. 1, the MFIR relaxation time course observed for a 1-mm thick slice was well-modeled as mono-exponential, yielding an estimated T_1 essentially equal to that estimated for the bulk sample, 2.8 s *vs.* 2.7 s, respectively. However, deviation from mono-exponential relaxation became increasingly apparent as slice thickness decreased. This can be illustrated using standard deviations of the residuals from these fits as a goodness-of-fit metric (Table 1). Further, Bayesian analysis was used to determine the probabilities of mono-, bi-, and tri-exponential models for each data set. A mono-exponential model was the most probable for data obtained at slice thicknesses of 1.00 and 0.500 mm, and a bi-exponential model was most probable for data obtained at slice thicknesses of 0.250 and 0.125 mm (Table 1). This bi-exponentiality is clearly illustrated in Fig. 2 (TH = 0.125 mm). Apparent longitudinal relaxation time constants, computed from mono-exponential and bi-exponential fits to the MFIR data obtained from slices with different thicknesses, are shown in Table 2. The apparent longitudinal relaxation time computed from a mono-exponential fit decreases as slice thickness decreases (Table 2).

Within a thin slice, the observed relaxation time course was non-mono-exponential. While such time-course data are well-modeled as bi-exponential (Fig. 2, Tables 1 and 2), neither of the bi-exponential decay time constants corresponds to the "true" longitudinal relaxation time constant. For example, bi-exponential modeling of MFIR data from a 0.125-mm thick slice yielded time-constant estimates of 2.2 ± 0.2 s and 0.17 ± 0.02 s with component fractional amplitudes of 0.68 and 0.32, respectively. Both time-constant estimates are substantially different from the bulk sample T_1, 2.7 s.

3.2. Fiber phantom experiments

3.2.1. Non-permeable fiber

For the non-permeable fiber phantom, water ^{1}H T_1 maps of the region surrounding the fiber (extra-fiber space) in the presence or absence of gadodiamide solution (0 and 1 mM) were homogeneous, with a mean relaxation time constant that agreed with spectroscopic (non-imaging) measurements (~3 s and ~0.2 s, respectively). In the presence of lumenal flow, the lumenal water spin-echo signal intensity decreased to the noise level, independent of gadodiamide concentration (0 and 1 mM).

3.2.2. Semi-permeable fiber/absence of flow

For the semi-permeable fiber phantom in the absence of flow, water ^{1}H T_1 maps in the absence or presence of gadodiamide solution (0 and 1 mM) were homogeneous. As expected, T_1 was markedly shortened in the presence of 1-mM gadodiamide solution (~0.2 s). In response to the observation that the T_1 of water in the fiber wall was the same as in the other compartments, magnetization-transfer (MT) experiments were performed (data not shown) that revealed no MT between fibers and water. Proton-density-weighted images and the individual images acquired for T_1-mapping clearly defined the region of the fiber wall (e.g., Fig. 3, panel C).

3.2.3. Semi-permeable fiber/presence of flow/absence of gadodiamide

For the semi-permeable fiber phantom in the presence of flow but without gadodiamide, apparent T_1 values varied as a function of voxel distance from the lumen boundary. Fig. 3 shows a T_1 map, as well as a gradient-echo image identifying fiber-wall position. Compared to T_1 measured in the absence of flow, the presence of lumenal flow results in shorter T_1 values in voxels near the fiber, an effect most pronounced within the fiber wall. Moving radially away from the fiber wall, voxel T_1 values lengthen, returning to 95% of that observed in the absence of flow at a distance of 120 μm from the outer edge of the fiber wall. The lengthening of T_1 was well fit by a mono-exponential dependence on radial distance from the fiber wall. The exponential coefficient k governing this spatial change in T_1 (modeled from the combined data shown in Fig. 3, Panel B; solid line) was 0.018 ± 0.003 μm^{-1} (or equivalently, 0.36 ± 0.05 voxel^{-1}).

As described in Section 2, an ROI covering one sixteenth of the entire image (0.64 × 0.64 mm^2; 976 voxels after thresholding to remove lumenal voxels) was selected, with the fiber at its center, and the relaxation time course for this entire ROI was derived from knowledge of the individual voxel T_1 values, Fig. 4. The derived ROI relaxation time-course data were preferentially modeled as bi-exponential. Bayesian model selection probabilities (P), expressed as natural log P, were −7.78, −0.232, −1.63, and −4.95 for mono-, bi-, tri- and quad-exponential models, corresponding to probabilities of ~0%, 79%, 20%, and 1%, respectively.

3.2.4. Semi-permeable fiber/presence of flow and gadodiamide

For the semi-permeable fiber phantom in the presence of lumenal flow and gadodiamide (1 mM), variation in voxel T_1 with distance from the fiber was not observed, i.e., T_1 was homogeneous

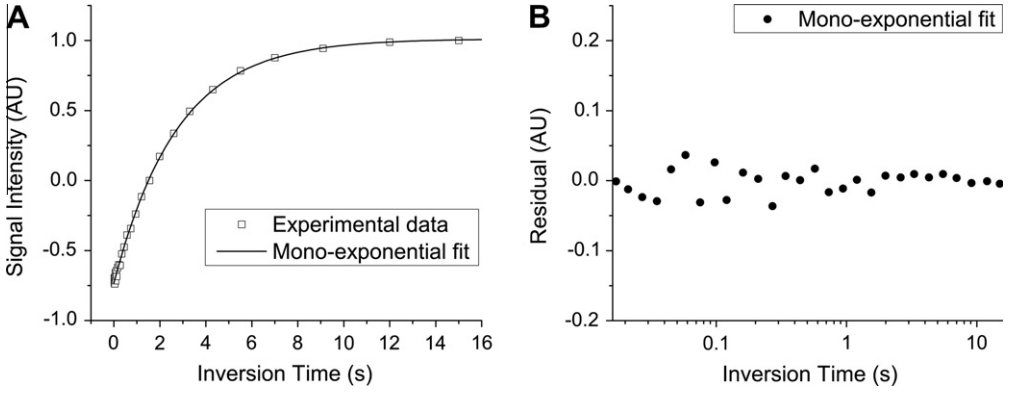

Fig. 1. Slice selection experiment: thick slice (TH = 1.00 mm). (A) Signal intensity *vs.* inversion time (TI); squares are experimental data values and the solid line corresponds to a mono-exponential model: SI(TI) = 1.012–1.744e$^{-TI/2.76}$. (B) Residuals from panel A *vs.* inversion time. (Note: inversion time axis is logarithmic.)

Table 1
Goodness-of-fit, expressed as the residual standard deviation, assuming either mono-exponential or bi-exponential fits to the data, for different slice thicknesses. A decrease in the residual standard deviation corresponds to a better fit. A decrease in the ratio of the values corresponds to the mono-exponential being preferred (more probable model).

$\sigma_{residual}$	TH = 1.00 mm	TH = 0.500 mm	TH = 0.250 mm	TH = 0.125 mm
Mono-exp	0.0196 ± 0.0005	0.0169 ± 0.0004	0.047 ± 0.001	0.110 ± 0.003
Bi-exp	0.0197 ± 0.0005	0.0156 ± 0.0006	0.029 ± 0.001	0.033 ± 0.001
Ratio[a]	1.0	1.1	1.6	3.3
$Probability_{mono}$[b,c]	-3.8×10^{-3}	-7.1×10^{-3}	−8.5	−8.5
$Probability_{bi}$[b,c]	−8.5	−8.5	-2.8×10^{-2}	-9.2×10^{-3}
$Probability_{tri}$[b,c]	−8.5	−8.5	−3.7	−4.9

[a] The ratio of the standard deviation of the residual with a mono-exponential fit to the standard deviation of the residual with a bi-exponential fit.
[b] Probabilities are those estimated by Bayesian analysis.
[c] Expressed as log base e of the probability.

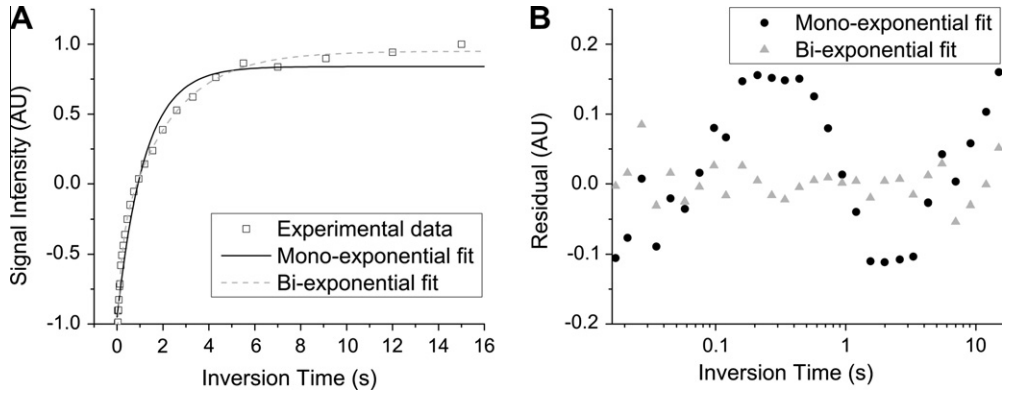

Fig. 2. Slice-selection experiment: thin slice (TH = 0.125 mm). (A) Signal intensity *vs.* inversion time; squares are data values, the solid line corresponds to a mono-exponential model: $SI(TI) = 0.84–1.79e^{-TI/1.2}$ and the dashed line corresponds to a bi-exponential model: $SI(TI) = 0.95–1.40e^{-TI/2.2} - 0.65e^{-TI/0.17}$. (B) Residuals from panel A *vs.* inversion time; circles denote the mono-exponential model and triangles the bi-exponential model. (Note: inversion time axis is logarithmic.)

throughout. However, as for the no-flow case, voxel T_1 values were shortened markedly (~0.2 s) compared with the situation in which gadodiamide was absent (~3 s).

4. Discussion

Perfusion-sensitive MR methods, such as arterial spin labeling (ASL) and dynamic contrast enhanced (DCE) MRI, are valuable techniques for the detection and staging of illness and disease. However, these techniques only reach their full potential when derived parameter estimates are quantitative (i.e., accurate and precise). When using a signal model employing a single R_1 value (i.e., mono-exponential longitudinal relaxation), both ASL and DCE-MRI implicitly assume the presence of well-mixed compartments. Errors in parameter estimates occur with deviations from mono-exponential relaxation. As described previously by others, such deviations are observed for systems in which the detected signal arises from multiple, internally well-mixed compartments that are not in fast exchange [15–17]. The examples presented in this paper demonstrate that deviations from mono-exponential longitudinal relaxation can also be detected when the signal arises from a poorly mixed single compartment, due to diffusion of spins from a communicating second compartment (physical or virtual). In many ways, these deviations are similar to those resulting from inflow [18].

The slice-thickness experiment separated a homogeneous phantom (single physical compartment) into two virtual compartments, consisting of spins either initially inside or outside the selected inversion slice. Signal was then observed only from magnetization inside the selected inversion slice. Deviations from mono-exponential longitudinal relaxation were most dramatic when TH = 0.125 mm (Fig. 2). These deviations were not due to errors in slice profile, which were themselves minimized by crusher gradients and shaped RF pulses, as residual errors in slice profile would not result in non-mono-exponential relaxation with MFIR [7]. Rather, non-mono-exponential longitudinal relaxation occurred due to diffusion of a population of thermal-equilibrium-state spins (non-inverted bulk magnetization) from the second, virtual compartment into the selected slice and, correspondingly, diffusion of a population of non-thermal-equilibrium-state spins (inverted bulk magnetization) out of the slice. Decreasing the slice thickness decreased the number of spins initially in the slice, increasing the population of detected spins originating from outside the slice relative to the population of detected spins originating and remaining inside the slice. With decreasing slice thickness,

Table 2
Apparent longitudinal relaxation time constants, assuming either mono-exponential or bi-exponential fits to the data, for different slice thicknesses. These values are to be compared with the "true" T_1 value of 2.708 ± 0.002 s.

$T_{1,app}$	TH = 1.00 mm	TH = 0.500 mm	TH = 0.250 mm	TH = 0.125 mm
Mono-exp	2.76 ± 0.05 s	2.56 ± 0.04 s	2.00 ± 0.09 s	1.2 ± 0.1 s
Bi-exp	3 ± 1 s	2.7 ± 0.5 s	2.9 ± 0.4 s	2.2 ± 0.2 s
	1.1 ± 0.8 s	0.5 ± 0.5 s	0.6 ± 0.1 s	0.17 ± 0.02 s

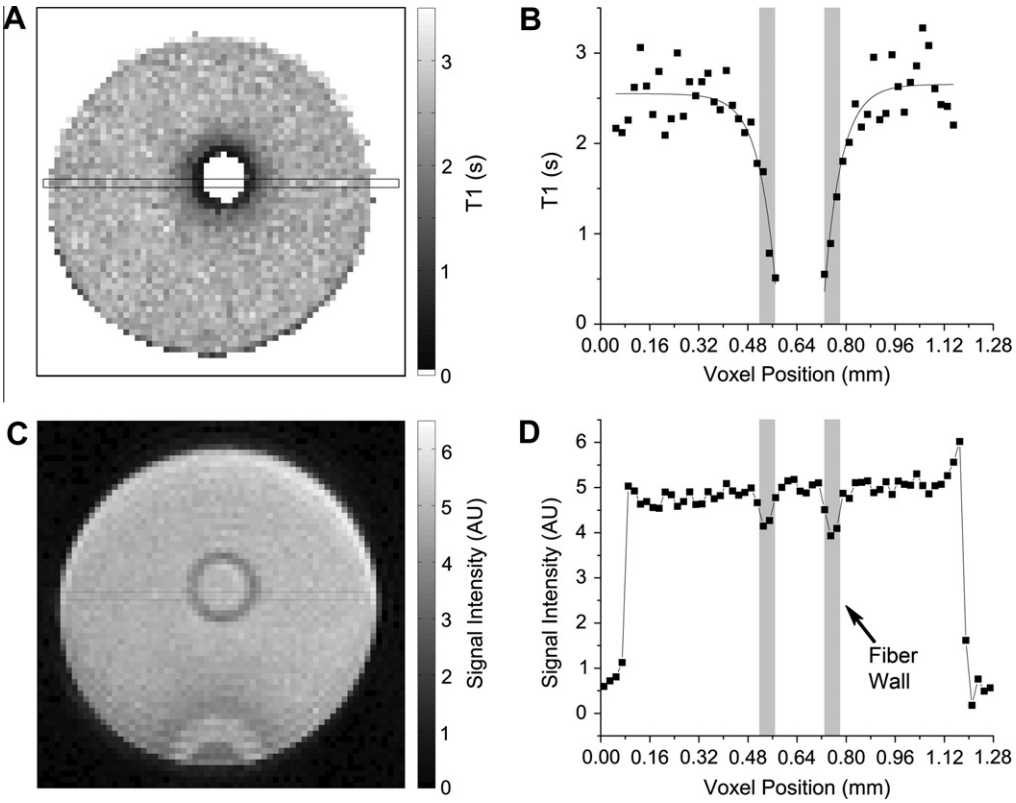

Fig. 3. Semi-permeable fiber (absence of gadodiamide). (A) Longitudinal relaxation time-constant (units expressed as s) map of the phantom with lumenal flow. (B) Longitudinal relaxation time constant *vs.* voxel position from a single line of the image as indicated in panel A where the data selected are within the outlined narrow rectangle. A mono-exponential fit (solid line in panel B; left side, $2.54–2.1e^{-0.018\times}$; right side, $2.64–2.3e^{-0.018\times}$) and gray shading rectangles denoting the location of the fiber walls are also shown. (C) Proton-density-weighted gradient-echo image of the same phantom, without lumenal flow, included for visualization of the fiber wall. (The artifact at the bottom of the image is from the susceptibility effect of an out-of-slice air bubble attached to the wall of capillary tube.) (D) Signal intensity *vs.* voxel position from a single line of the image shown in panel C, where the selected data are within the outlined narrow rectangle. Gray shading rectangles denote the location of the fiber wall.

Bayesian model selection analysis increasingly favors (more probable model) a bi-exponential characterization of the relaxation data, Table 1. Indeed, for the 0.250 and 0.125 mm thick slices, Bayesian model selection overwhelmingly favors the bi-exponential relaxation model compared to mono- or tri-exponential models. Likewise, consistent with the Bayesian model selection, qualitative examination of the residuals, presented in Table 1, illustrates that there is no improvement in bi-exponential *vs.* mono-exponential fitting of the thick-slice relaxation data, but marked improvement for the thin-slice relaxation data. Concomitantly, when a mono-exponential model is used to fit the data, absolute error (i.e., the deviation of the computed longitudinal relaxation time from its true value) increases as slice thickness is decreased.

This example of diffusion-driven longitudinal relaxation is expected to result in a broad distribution of relaxation rates, with spin populations at the very edge of the slice having the greatest diffusion-driven-contribution to relaxation and those spin populations in the middle of the slice having the least diffusion-driven-contribution to relaxation. Although a broad distribution of relaxation rates is expected, the single-slice-relaxation

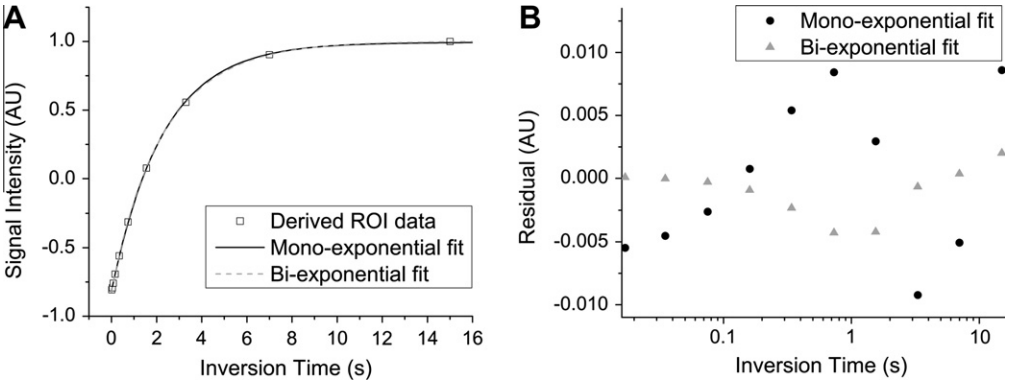

Fig. 4. Semi-permeable fiber (presence of flow, absence of gadodiamide) derived ROI data. (A) Derived ROI signal intensity *vs.* inversion time; squares are derived data values, the solid line corresponds to a mono-exponential model: $SI(TI) = 0.99–1.8e^{-TI/2.3}$, and the dashed line corresponds to a bi-exponential model: $SI(TI) = 1.00–1.7e^{-TI/2.5} – 0.13e^{-TI/0.82}$. (B) Residuals from panel A *vs.* inversion time; circles denote the mono-exponential model and triangles the bi-exponential model. (Note: inversion time axis is logarithmic.)

spectroscopy data (sum of all spin populations) are remarkably well-modeled as "simply" bi-exponential, even for the thinnest slice examined (TH = 0.125 mm). It is worth noting that for the thinnest slice, TH = 0.125, neither exponential time constant, 2.2 ± 0.2 s nor 0.17 ± 0.02 s, corresponds to the true spin–lattice relaxation time constant, 2.7 s. Furthermore, the measured fractional amplitudes and component time constants depend upon slice thickness. As slice thickness increases and diffusion-driven relaxation becomes less significant, the fractional amplitude of the rapidly relaxing component decreases toward zero, the time constant for the slowly relaxing component approaches that of the true spin–lattice relaxation time constant, and relaxation appears mono-exponential (Table 2).

While the manner in which a bi-exponential function can well-approximate signals that are, *a priori*, more complex, is a recurring theme in MR data analysis, diffusion-driven bi-exponential relaxation is not limited to experiments utilizing thin slices, as is demonstrated herein with thick slices and the semi-permeable fiber phantom.

Control experiments with the non-permeable fiber phantom in the presence and absence of flow and the semi-permeable fiber phantom in the absence of flow were well-characterized by spatially homogeneous, mono-exponential relaxation maps of the extra-fiber space (more precisely, in the case of the semi-permeable fiber phantom, extra-lumenal space). Further, imaging-derived voxel T_1 values agreed with T_1 values obtained by spectroscopic methods. Likewise, the semi-permeable fiber phantom in the presence of flow and 1 mM gadodiamide was well-characterized by a spatially homogeneous, mono-exponential, relaxation map of the extra-lumenal space with voxel T_1 values markedly shortened (~0.2 s) from values obtained in the absence of gadodiamide (~3 s). Thus, (i) in the absence of flow or (ii) in the presence of flow but the absence of diffusion-driven magnetization exchange or (iii) when relaxation in a directly detected compartment is sufficiently rapid relative to exchange between compartments (*vide infra*), irrespective of the presence of flow or diffusion-driven magnetization exchange, extra-fiber relaxation is spatially uniform and mono-exponential in nature.

The situation is quite different for the case of the semi-permeable fiber phantom in the presence of flow, but the absence of gadodiamide. Here, spatially-inhomogeneous relaxation is observed for the extra-lumenal space, with T_1 values dependent on the distance from the lumenal boundary (see Fig. 3 panel B, modeled curve). Recall that no signal is observed for spins remaining within the lumen because of time-of-flight, spin-echo signal suppression. Variations in T_1 are, therefore, due to diffusion of thermal-equilibrium-state spin populations from the lumenal compartment to the extra-lumenal compartment and concomitant diffusion of partially saturated spin populations from the extra-lumenal compartment to the lumenal compartment. T_1 shortening is most pronounced in the fiber wall and dies away with increasing radial distance from the lumen boundary. This effect is independent of slice thickness.

The summed signal from an ROI with the fiber at its center (see Section 2) will include voxels having different T_1 values and, thus, will be characterized, *a priori*, by multi-exponential relaxation behavior. Nevertheless, the derived ROI data are seen to be fit preferentially to a bi-exponential model. It is worth noting that neither resulting exponential time constant, 2.5 s nor 0.82 s, corresponds to the true spin–lattice relaxation time constant, 2.7 s. Likewise, the fractional amplitudes and component time constants will vary with the size and position of the ROI relative to the fiber location.

Returning briefly to the case of the semi-permeable fiber in the presence of flow and gadodiamide, recall that, for parallel kinetic processes, rate constants (not time constants) are additive. The presence of 1 mM gadodiamide dominates water relaxation to the extent that the additional relaxation pathway provided by diffusion-driven exchange makes only a minor, essentially undetectable, contribution. For example, consider the innermost voxels associated with the fiber wall (i.e., voxels immediately adjacent to those in the fiber lumen), where diffusion-driven relaxation contribution is maximal (Fig. 3.). In the absence of gadodiamide but in the presence of flow, the longitudinal relaxation rate constant increased from 0.38 s^{-1} to 1.88 s^{-1}, an additive diffusion-driven contribution of 1.50 s^{-1}. In the presence of 1 mM gadodiamide and flow, this additive diffusion-driven relaxation contribution is predicted to increase the rate constant from 4.3 s^{-1} to 5.8 s^{-1}, a decrease to the time constant of 0.06 s. However, for the semi-permeable fiber in the absence of flow but in the presence of gadodiamide, the average T_1 in the extra-lumenal space was 0.23 ± 0.06 s. Thus, in the presence of 1 mM gadodiamide, the expected maximal relaxation contribution from diffusion in the presence of flow falls within the error of the measurement in the absence of flow (i.e., is undetectable).

5. Conclusions

As scanner technology advances, MR experiments performed with phantoms allow for the testing and modeling of biophysical phenomena with unprecedented accuracy and precision. The two "simple" phantoms and associated experiments described herein are part of such an effort, relating to dynamic contrast enhancement and flow/perfusion measurement protocols. However, even such simple phantoms and relatively uncomplicated MR protocols yield multi-exponential relaxation data. Further, the data – while *a priori* clearly multi-exponential – are well approximated as bi-exponential, a consistent theme with MR relaxation data of realistic SNR.

These experiments specifically highlight the effects of diffusion-driven exchange on careful relaxation measurements and serve as another cautionary reminder about the risks of over-interpretation of bi-exponential data [19,20]. When bi-exponential signals are observed in MR, it is tempting to ascribe physical/physiologic significance – such as unique compartments – to the component fractional amplitudes and decay-rate constants. As demonstrated in both the thin-slice and single-fiber experiments, this need not be the case.

Acknowledgments

Support from NIH grants T90 DA22871, R01 EB002083, P30 CA91842, S10 RR022658, and S10 RR020916 is gratefully acknowledged.

References

[1] M.D. Does, C. Beaulieu, P.S. Allen, R.E. Snyder, Multi-component T1 relaxation and magnetisation transfer in peripheral nerve, Magn. Reson. Imaging 16 (1998) 1033–1041.
[2] M.D. Does, J.C. Gore, Compartmental study of T1 and T2 in rat brain and trigeminal nerve in vivo, Magn. Reson. Med. 47 (2002) 274–283.
[3] W.B. Hyslop, P.C. Lauterbur, Effects of restricted diffusion on microscopic NMR imaging, J. Magn. Reson. 94 (1991) 501–510.
[4] H.D. Morris, W.B. Hyslop, P.C. Lauterbur, Diffusion-enhanced NMR microscopy, in: Proc. Soc. Magn. Reson., San Francisco, 1994, pp. 376.
[5] A.M. Prantner, G.L. Bretthorst, J.J. Neil, J.R. Garbow, J.J.H. Ackerman, Magnetization transfer induced biexponential longitudinal relaxation, Magn. Reson. Med. 60 (2008) 555–563.
[6] R.K. Gupta, J.A. Ferretti, E.D. Becker, G.H. Weiss, A modified fast inversion-recovery technique for spin–lattice relaxation measurements, J. Magn. Reson. 38 (1980) 447–452.
[7] J.L. Evelhoch, J.J.H. Ackerman, NMR T1 measurements in inhomogeneous B1 with surface coils, J. Magn. Reson. 53 (1983) 52–64.
[8] P.B. Kingsley, Methods of measuring spin–lattice (T1) relaxation times: an annotated bibliography, Concepts Magn. Reson. 11 (1999) 243–276.

[9] M.A. Bernstein, K.F. King, X.J. Zhou, Handbook of MRI Pulse Sequences, Academic Press, Amsterdam, Boston, 2004.
[10] M. Shinnar, L. Bolinger, J.S. Leigh, The synthesis of soft pulses with a specified frequency response, Magn. Reson. Med. 12 (1989) 88–92.
[11] G.L. Bretthorst, W.C. Hutton, J.R. Garbow, J.J.H. Ackerman, Exponential parameter estimation (in NMR) using Bayesian probability theory, Concepts Magn. Reson. A (Magn. Reson. Eng.) 27A (2005) 55–63.
[12] G.L. Bretthorst, W.C. Hutton, J.R. Garbow, J.J.H. Ackerman, Exponential model selection (in NMR) using Bayesian probability theory, Concepts Magn. Reson. A (Magn. Reson. Eng.) 27A (2005) 64–72.
[13] G.L. Bretthorst, Automatic phasing of MR images. Part I: Linearly varying phase, J. Magn. Reson. 191 (2008) 184–192.
[14] G.L. Bretthorst, Automatic phasing of MR images. Part II: Voxel-wise phase estimation, J. Magn. Reson. 191 (2008) 193–201.
[15] K.M. Donahue, R.M. Weisskoff, D. Burstein, Water diffusion and exchange as they influence contrast enhancement, J. Magn. Reson. Imaging 7 (1997) 102–110.
[16] T.E. Yankeelov, W.D. Rooney, X. Li, C.S. Springer Jr., Variation of the relaxographic ‘‘shutter-speed’’ for transcytolemmal water exchange affects the CR bolus-tracking curve shape, Magn. Reson. Med. 50 (2003) 1151–1169.
[17] X. Li, W.D. Rooney, C.S. Springer Jr., A unified magnetic resonance imaging pharmacokinetic theory: intravascular and extracellular contrast reagents, Magn. Reson. Med. 54 (2005) 1351–1359.
[18] J.H. Lee, X. Li, M.K. Sammi, C.S. Springer Jr., Using flow relaxography to elucidate flow relaxivity, J. Magn. Reson. 136 (1999) 102–113.
[19] D.A. Yablonskiy, G.L. Bretthorst, J.J. Ackerman, Statistical model for diffusion attenuated MR signal, Magn. Reson. Med. 50 (2003) 664–669.
[20] M.L. Milne, M.S. Conradi, Multi-exponential signal decay from diffusion in a single compartment, J. Magn. Reson. 197 (2009) 87–90.